Three-Dimensional Auxetic Porous Medium

Antonio Baldi, Michele Brun* and Giorgio Carta

Dipartimento di Ingegneria Meccanica, Chimica e dei Materiali, Università degli Studi di Cagliari, Piazza d'Armi, 09123 Cagliari, Italy

Abstract

We propose the design of a novel three-dimensional porous continuous solid exhibiting negative Poisson's ratio. The shape and periodic distribution of the pores guarantee cubic symmetry, and the directional dependance of the Poisson's ratio and Young's modulus shows a moderate degree of anisotropy and multidirectional *auxeticity*. We demonstrate the auxeticity of the porous solid numerically, solving both a periodic analysis on a unit cell and a boundary value problem on a finite specimen. The numerical results are fully confirmed by experimental results, obtained from Digital Image Correlation data. The final parametric analysis indicates how to modulate the characteristic parameters of the microstructure in order to tune macroscopic properties. The proposed design maintains a relatively high Young's modulus and it is prone to large-scale industrial production.

*Corresponding author (e-mail address: mbrun@unica.it)

Keywords: Negative Poisson's ratio, Auxetic Material, Porous Medium, Digital Image Correlation.

1 Introduction

The Poisson's ratio [68], the negative ratio between transverse and longitudinal deformations, is a measure of the ratio between the bulk modulus K and the shear

modulus μ and gives an indication of the tendency of a solid to deform by resisting mainly to changes in volume or shape. It is well-known that, for a stable linear elastic isotropic material, the Poisson's ratio ν is limited from above by 0.5 for an incompressible material, where $K/\mu \to \infty$, and from below by the stability limit -1, where $K/\mu \to 0$; two limits which are not present in the anisotropic cases [83, 65].

Materials with negative Poisson's ratio, commonly addressed as *auxetic* (from Evans [25, 27]), expand in the direction perpendicular to the applied tensile stress and contract for perpendicular compressive stress.

Auxetic materials are known to provide higher indentation resistance [47, 33] and fracture toughness [9, 22, 29], relatively low bulk and high shear stiffness [32, 78], significant acoustic [42, 66] and impact [39] energy absorption, deformation-dependent permeability [2], large resistance to fiber pullout [91], natural coupling with negative thermal expansion [38, 13, 71] and enhanced formability due to sinclastic or dome-shape curvature under bending [19, 26].

Due to the above-mentioned properties, there is an increasing interest in negative Poisson's ratio materials concerning technological applications: they include, among the others, stent technology [62, 10, 55] and tissue engineering [59, 87, 77], where the mechanical characteristics of auxetic engineered media match or even enhance the mechanical properties of healthy normal host tissues, permitting full functionality and enabling them to fulfil their role *in vivo*; impact protection [24, 28, 70], where auxeticity aids energy absorption, peak force attenuation and indentation resilience; sensors [20, 51] and actuators [45, 50], where high-compressibility and formability are key properties.

Naturally-occurring auxetic behaviour has been discovered both in inorganic materials such as iron pyrites [56], arsenic and bismuth [37], cadmium [53], several cubic and face-centred cubic rare gas solids along a specific crystallographic direction [7], and in a number of biological tissues such as in cats' [84] and cows' [52] teat skins, cancellous bones [89], embryonic epithelial tissues [88], arteries [82], tendons [31] and the annulus fibrosus of the intervertebral disc [21].

Nevertheless, the main attention has been devoted to the design of artificially-architected materials, which is sustained by the dramatic advances in processing techniques (polymer-based templating and direct single- or multi-material formation). The design of the microstructure exploits different geometries and mechanisms, which are reviewed in [33, 72, 48, 1]. We report here re-entrant unit cells [46, 54, 67], star-shaped inclusions [81, 63], chiral configurations [69, 35, 5], topologically-optimised microstructures [75, 49, 76], perforations and cuttings [36, 80, 73, 14, 15, 64], rotating rigid units [34, 60, 61], lattices [11, 12, 17] and elastic instabilities [8].

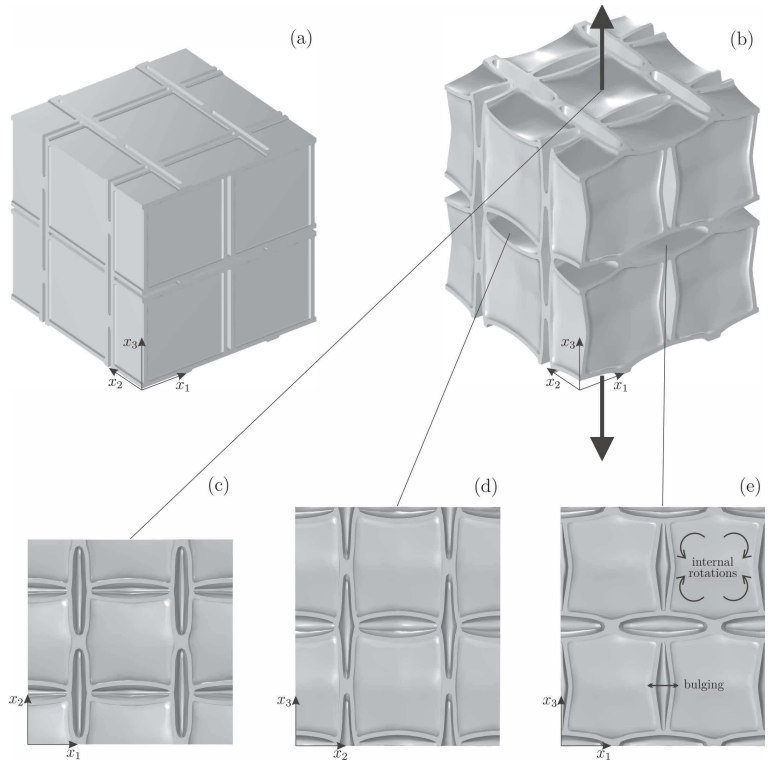

Figure 1: Finite specimen of a three-dimensional porous medium subjected to uniaxial tension in x_3-direction. The geometry of the specimen and constitutive properties of the matrix are the same as in Sections 4 and 5. Initial and deformed configurations of the central $2 \times 2 \times 2$ cells are shown in parts (a) and (b), respectively. For the deformed configuration: (c) top view, (d) side view, (e) front view.

In the last decade, there has been a strong effort in the design of fully three-dimensional microstructures, which are not obtained from simple extrusion of a planar geometry: in the quasi-totality of the cases they are lattice structures [3, 12, 30, 85, 92], with few exceptions concerning foams [23, 92], woven fabrics [44] and voided elastomers [4, 74], both with very high porosity. Some designs may reach low Poisson's ratios: among isotropic models, in [12] it is reported a omni-directional Poisson's ratio equal to -0.41; on the other hand, anisotropic designs can lead to Poisson's coefficients close [58] or even lower [12, 86, 30] than -1 along specific orientations.

However, lattices and foams are generally characterized by significantly small values of the Young's moduli. In addition, lattice structures are manufactured with technologies which are not prone to large-scale industrial production (in the quasi-totality of the cases, 3D printing technologies are employed). On the other hand, foams are random structures with good properties, which are not always easy to control. Conversely, a regular porous system combines high predictability of the macroscopic properties (due to the internal regular structure) and the possibility to pave the way to industrial applications since particulate and, specifically, porous composites are already produced at industrial level with, for example, a US market that is expected to reach USD 3.2 billion by 2028 [43].

In this paper, we propose a novel porous material, a continuous composite with a periodic three-dimensional microstructure exhibiting auxetic behavior. The microstructure does not derive from a simple extrusion of a two-dimensional geometry, but has fully three-dimensional nature. The particulate composite is characterized by cubic symmetry, so that auxeticity is omnidirectional; in addition, the low porosity (less than 20%) leads to a relatively large Young's modulus, which makes the composite suitable for technological applications where the structural response plays a significant role.

The macroscopic auxetic effect is the result of non-homogeneous deformations, localised in the neighbourhoods of the voids' centres. More specifically, the mutual interaction between voids induces a bulging (flattening) of the voids under tension (compression) and internal rotations in the solid phase. In Fig. 1 it is possible to appreciate qualitatively the internal mechanism leading to macroscopic auxeticity. A finite specimen, subjected to uniaxial tension in the x_3-direction, expands in the transverse x_1- and x_2-directions; the deformation of the central $2\times2\times2$ cells of the specimen, composed of $4\times4\times5$ cells, highlights that the expansion in transverse directions is driven by the bulging of the voids and internal rotations.

In this work we determine the effective properties of the porous medium both numerically and experimentally. The plan of the paper is as follows: in Section 2, we present the geometry of the microstructure, followed, in Section 3, by the analytical and numerical determination of the effective properties of the periodic

system, with the study of the directional dependence of the macroscopic material parameters. In Section 4, we describe the experimental procedure, briefly detailing the statistical analysis of the experimental data. The comparison between the experimental and numerical data is shown in Section 5, with an additional numerical simulation of the experimental sample. In Section 6, we report a parametric analysis of the effective properties as functions of the microstructural geometric parameters, while concluding remarks are given in Section 7.

2 Geometry of the microstructured auxetic medium

In this section, we present the design of the microstructure of the porous medium, where the shape and the periodic distribution of the void inclusions are responsible for the negative effective Poisson's ratio.

2.1 Shape and distribution of the voids

As shown in Fig. 2b, each void presents a parallelepiped shape having square base, with height t and side length of the square base a, where $a \gg t$. In order to reduce stress concentration, the parallelepiped-shaped void is rounded in proximity of the thin lateral faces and the short edges.

The position of each void is determined by the vector $\boldsymbol{x}_C^{(i)}$, defining the coordinates of the centre $C^{(i)}$ (see Fig. 2a). The orientation of the void is specified by the unit normal vector $\boldsymbol{n}^{(i)}$, perpendicular to the square base, and by the unit tangential vector $\boldsymbol{t}^{(i)}$, parallel to one edge of length a. The superscript i takes the values 1, 2 or 3 since there are three sets of voids, as discussed in Section 2.2. Note that the distance between coplanar void inclusions is $2l$–$(a + t)$, while the coalescence limit introduces the constraint $2l > (a + \sqrt{2}t)$.

2.2 Description of the periodic system

The periodic medium is made of cubic unit cells of side length $2l$. The set of lattice vectors Λ defining the periodic structure is given by

$$\Lambda = \{\boldsymbol{R} : \boldsymbol{R} = 2l(p\boldsymbol{e}_1 + q\boldsymbol{e}_2 + r\boldsymbol{e}_3), \quad p, q, r \in \mathbb{Z}\} \ . \tag{1}$$

Three periodic sets of voids are embedded in the continuous matrix. The shape of each void is illustrated in Figs. 2a and 2b. Each set $\Omega^{(i)}$, with $i = 1, 2, 3$ here and

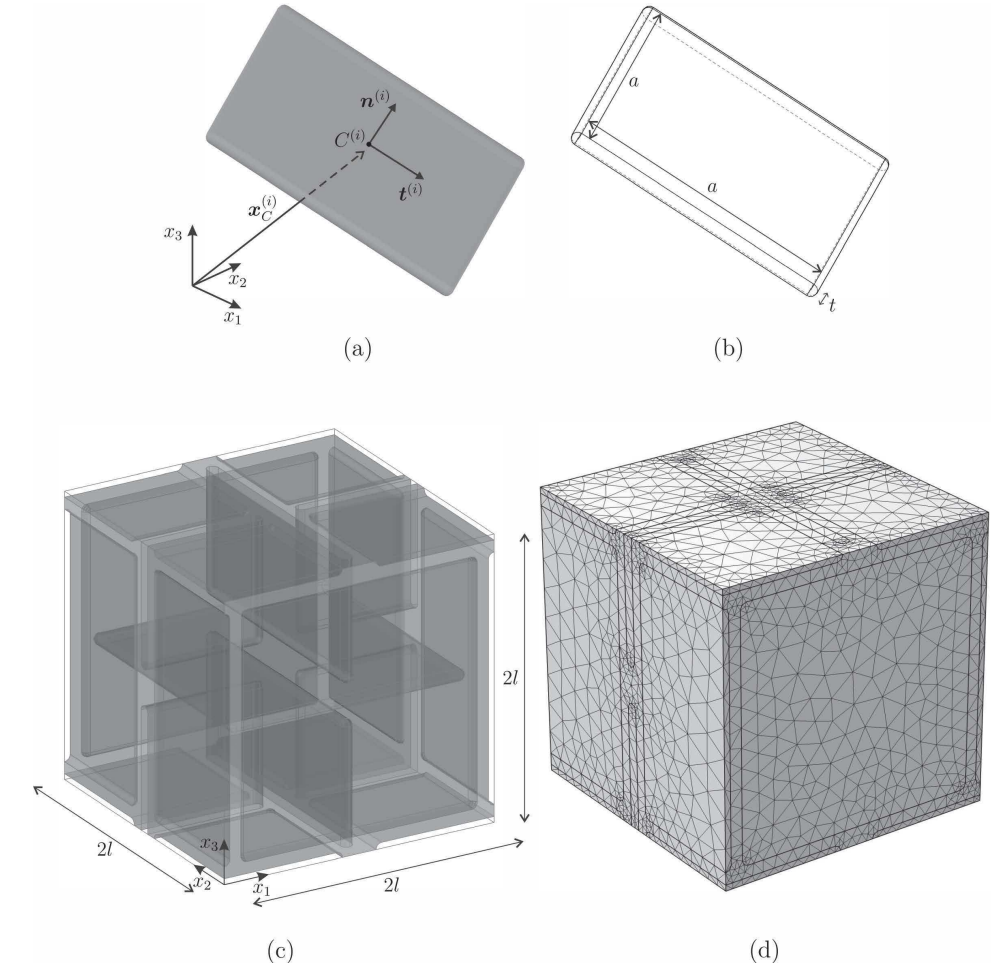

Figure 2: Design of the unit cell. (a) Schematic representation of each void, where $\boldsymbol{x}_C^{(i)}$ is the position vector of the centre of the void $C^{(i)}$, and $\boldsymbol{n}^{(i)}$ and $\boldsymbol{t}^{(i)}$ $(i = 1, 2, 3)$ are the normal and tangential vectors, respectively. (b) Dimensions of the parallelepiped-shaped void inclusions: t and a denote the height and the side length of the square base, respectively. (c) Unit cell of the periodic porous medium, having cubic shape with side length $2l$. The holes are coloured in grey. (d) Optimised mesh used in the numerical computations.

in the following, is characterized by unit normal vector $\boldsymbol{n}^{(i)} = \boldsymbol{e}_i$, unit tangential vector $\boldsymbol{t}^{(i)} = \boldsymbol{e}_j$ or $\boldsymbol{e}_k$ $(i \neq j \neq k \neq i)$ and central points

$$C^{(1)} = (l, l, 0), \quad C^{(2)} = (0, l, 0), \quad C^{(3)} = (0, 0, 0). \tag{2}$$

The voids have different periodicity than the unit cell; the lattice vectors λ_i for the three set of voids are expressed by

$$\begin{aligned}
\lambda_1 &= \{\boldsymbol{R} : \boldsymbol{R} = l[2p\boldsymbol{e}_2 + 2q\boldsymbol{e}_3 + r(\boldsymbol{e}_1 + \boldsymbol{e}_2 + \boldsymbol{e}_3)]\} \,, \\
\lambda_2 &= \{\boldsymbol{R} : \boldsymbol{R} = l[2p\boldsymbol{e}_3 + 2q\boldsymbol{e}_1 + r(\boldsymbol{e}_1 + \boldsymbol{e}_2 + \boldsymbol{e}_3)]\} \,, \\
\lambda_3 &= \{\boldsymbol{R} : \boldsymbol{R} = l[2p\boldsymbol{e}_1 + 2q\boldsymbol{e}_2 + r(\boldsymbol{e}_1 + \boldsymbol{e}_2 + \boldsymbol{e}_3)]\} \,, \qquad p, q, r \in \mathbb{Z} \,.
\end{aligned} \tag{3}$$

The unit cell of the periodic medium is shown in Fig. 2c, where the matrix phase has been made transparent to show all the pores inside the cell.

3 Effective properties of the periodic system

Here, we determine the effective elastic properties of the periodic porous auxetic medium described in Section 2.2. The auxetic porous medium is a cubic material, since both the matrix and the pores are isotropic and considering that the geometry has cubic symmetry.

In the linear elastic regime, the material behaviour is determined when three elastic constants, namely the effective Poisson's ratio ν^*, the effective Young's modulus E^* and the effective shear modulus μ^*, are known. They can be computed from macroscopic stress $\bar{\boldsymbol{\sigma}}$ and deformation $\bar{\boldsymbol{\varepsilon}}$ components, along the principal directions of the composite, as follows:

$$\nu^* = \frac{(\mathrm{tr}\{\bar{\boldsymbol{\varepsilon}}\} - \bar{\varepsilon}_{ii})\bar{\sigma}_{ii} - (\mathrm{tr}\,\bar{\boldsymbol{\sigma}} - \bar{\sigma}_{ii})\bar{\varepsilon}_{ii}}{(\mathrm{tr}\{\bar{\boldsymbol{\varepsilon}}\} - \bar{\varepsilon}_{ii})(\mathrm{tr}\,\bar{\boldsymbol{\sigma}} - \bar{\sigma}_{ii}) - (\bar{\sigma}_{ii} + \mathrm{tr}\,\bar{\boldsymbol{\sigma}})\bar{\varepsilon}_{ii}} \,, \tag{4}$$

$$E^* = \frac{(\mathrm{tr}\,\bar{\boldsymbol{\sigma}} - 3\bar{\sigma}_{ii})\,\mathrm{tr}\,\bar{\boldsymbol{\sigma}}}{(\mathrm{tr}\{\bar{\boldsymbol{\varepsilon}}\} - \bar{\varepsilon}_{ii})(\mathrm{tr}\,\bar{\boldsymbol{\sigma}} - \bar{\sigma}_{ii}) - (\bar{\sigma}_{ii} + \mathrm{tr}\,\bar{\boldsymbol{\sigma}})\bar{\varepsilon}_{ii}} \tag{5}$$

and

$$\mu^* = \frac{\bar{\sigma}_{ij}}{2\bar{\varepsilon}_{ij}} \,, \tag{6}$$

for each $i, j = 1, 2, 3$, where $i \neq j$, i is not summed and tr is the trace operator.

3.1 Numerical computation of effective properties

The unit cell shown in Fig. 2c is modelled in the finite element software *Comsol Multiphysics* [18]. Dirichlet periodic conditions are imposed at the boundaries of the domain (see, for reference, [14]) and six additional degrees of freedom have been blocked in order to prevent rigid body motions. The mesh has been generated following a two-step procedure: first, symmetric boundary meshes have been created on opposite boundary faces; subsequently, the internal three-dimensional mesh has been built accordingly. The mesh size has been calibrated in order to assure a sufficient convergence of the results, with a total of $1.86 * 10^5$ tetrahedral elements. The optimised discretisation of the unit cell is shown in Fig. 2d.

We assume that the matrix is an isotropic linear elastic material, having Poisson's ratio $\nu_m = 0.35$ and Young's modulus $E_m = 3035$ MPa. The side length of the cubic unit cell is $2l = 30$ mm, and the voids have dimensions $a = 25$ mm and $t = 1.25$ mm. These parameters also characterise the real specimen tested in the laboratory (see Section 4).

To evaluate the effective Poisson's ratio ν^* and the effective Young's modulus E^*, we apply a macroscopic axial strain $\bar{\varepsilon}_{11} = 10^{-4}$, while the other macroscopic strain components are set to zero (macroscopic strains are imposed through the periodic boundary conditions). The numerical analysis provides the required components of the stress tensor, averaged over the unit cell in order to give macroscopic fields. In particular, since $\bar{\varepsilon}_{22} = \bar{\varepsilon}_{33} = 0$ and, due to the cubic symmetry, $\bar{\sigma}_{22} = \bar{\sigma}_{33}$[1], (4) and (5) simplify into

$$\nu^* = \frac{\bar{\sigma}_{22}}{\bar{\sigma}_{11} + \bar{\sigma}_{22}} \tag{7}$$

and

$$E^* = \frac{(\bar{\sigma}_{11} - \bar{\sigma}_{22})(\bar{\sigma}_{11} + 2\bar{\sigma}_{22})}{\bar{\varepsilon}_{11}(\bar{\sigma}_{11} + \bar{\sigma}_{22})}\,, \tag{8}$$

respectively.

For the choice of the parameters considered here, the effective Poisson's ratio is found to be $\nu^* = -0.171$. Consequently, the porous medium is auxetic. The numerical calculations yield an effective Young's modulus equal to $E^* = 577.8$ MPa.

Figure 3 shows the colour maps of the displacement components u_1, u_2 and u_3 along the three directions x_1, x_2 and x_3. The thin black lines represent the undeformed configuration of the model.

[1]The condition $\bar{\sigma}_{22} = \bar{\sigma}_{33}$ was verified numerically.

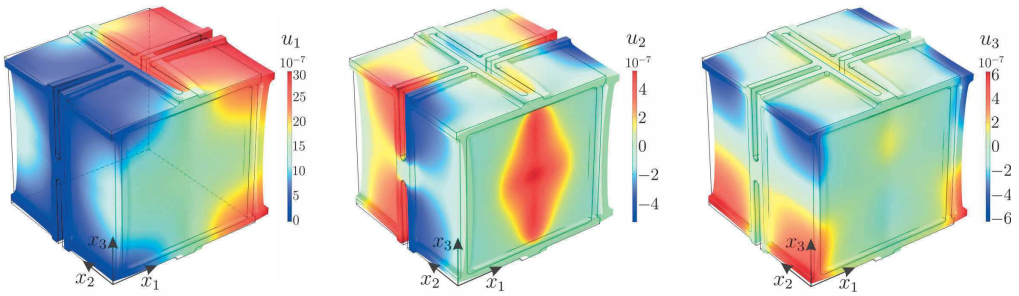

(a) (b) (c)

Figure 3: Displacement components in the unit cell of the periodic medium. The cell is subjected to the macroscopic axial strain $\varepsilon_{11} = 10^{-4}$. The displacement components are (a) u_1, (b) u_2 and (c) u_3.

In order to confirm the numerical results, we have performed two additional simulations, where the model has been subjected firstly to a macroscopic axial strain $\bar{\varepsilon}_{22} = 10^{-4}$ and secondly to $\bar{\varepsilon}_{33} = 10^{-4}$. The values of effective Poisson's ratio and Young's modulus obtained from these additional computations are identical to those found with the previously described simulation. Furthermore, imposing a macroscopic shear strain $\bar{\varepsilon}_{12} = 10^{-4}$, $\bar{\varepsilon}_{23} = 10^{-4}$ or $\bar{\varepsilon}_{31} = 10^{-4}$, we have determined an effective shear modulus equal to $\mu^* = 245.5$ MPa. Since

$$\mu^* \neq \mu^*_{iso} = \frac{E^*}{2(1+\nu^*)} = 348.5 \text{ MPa}, \tag{9}$$

the material is not isotropic.

3.2 Directional dependence of effective elastic constants

In Section 3.1 the effective Poisson's ratio ν^*, Young's modulus E^* and shear modulus μ^* are given along the principal directions of the composite material. For the anisotropic cubic material, it is of interest to understand the variation of the above effective properties in different directions.

Following [83, 12] for the computations of the coefficients of the constitutive tensor in a rotated frame of reference, the Young's modulus $E^*_{\boldsymbol{n}}$ along a generic direction $\boldsymbol{n}$ (with $|\boldsymbol{n}| = 1$) can be given in the form

$$E^*_{\boldsymbol{n}} = E^* \left[1 - 2(1+\nu^*) \left(1 - \frac{\mu^*_{iso}}{\mu^*} \right) (n_1^2 n_2^2 + n_1^2 n_3^2 + n_2^2 n_3^2) \right]^{-1}, \tag{10}$$

where $E^* = E^*_{(100)} = E^*_{(010)} = E^*_{(001)}$, with the subscripts indicating the crystallographic directions.

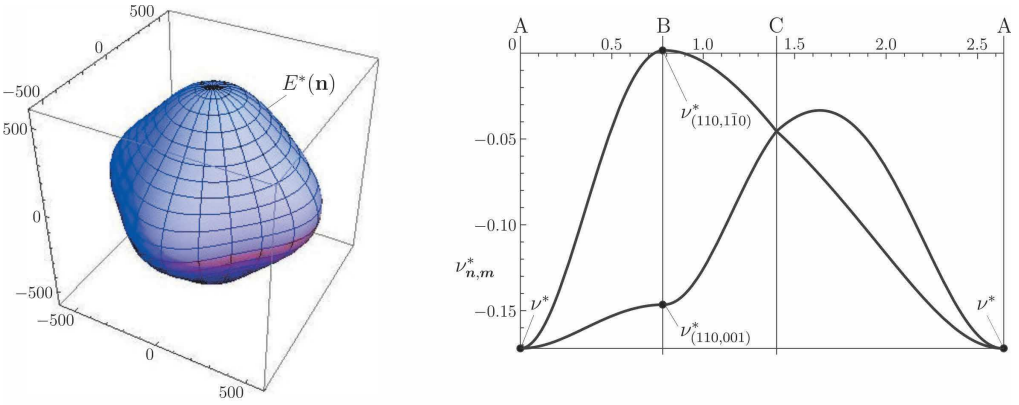

(a) (b)

Figure 4: (a) Polar representation of the effective Young's modulus $E^*(\mathbf{n})$. The values in the axes are given in MPa. (b) Extreme values of the effective Poisson's ratio $\nu^*_{\boldsymbol{n},\boldsymbol{m}}$ along the path $ABCA$ on the unit sphere $|\boldsymbol{n}| = 1$. The values $\nu^* = \nu^*_{min}$, $\nu^*_{(110,001)}$ and $\nu^*_{(110,1\bar{1}0)} = \nu^*_{max}$ are highlighted.

A further indication of the anisotropy of the porous composite is quantified by the dimensionless Zener anisotropy factor [90]

$$\beta_{cub} = \frac{\mu^*}{\mu^*_{iso}}, \tag{11}$$

which is equal to 1 for isotropic materials.

The value of the Young's modulus along different directions is shown in Fig. 4a. The variation of the Young's modulus, where $E^*_{max}/E^*_{min} = 1.23$ [2], together with the value of the Zener factor $\beta_{cub} = 0.704$, indicate that the composite has a "relatively small" anisotropy.

The variation of the Poisson's ratio is more involved, since $\nu^*_{\boldsymbol{n},\mathbf{m}}$ depends both on the direction of the applied load $\boldsymbol{n}$ and on the transverse direction $\boldsymbol{m}$, where $|\boldsymbol{m}| = 1$ and $\boldsymbol{m} \cdot \boldsymbol{n} = 0$. Depending on $\boldsymbol{n}$ and $\boldsymbol{m}$, the directional dependance of the Poisson's ratio is

$$\nu^*_{\boldsymbol{n},\boldsymbol{m}} = \frac{\nu^*\,\mu^* + (1+\nu^*)(\mu^* - \mu_{iso})(n_1^2 m_1^2 + n_2^2 m_2^2 + n_3^2 m_3^2)}{\mu^* - 2(1+\nu^*)(\mu^* - \mu_{iso})(n_1^2 n_2^2 + n_2^2 n_3^2 + n_3^2 n_1^2)}. \tag{12}$$

While in the isotropic case the Poisson's ratio is strictly bounded between -1 and 0.5, such bounds do not exist in the cubic case, and in [83] it is demonstrated that

[2] The maximum Young's modulus is $E^*_{max} = E^* = 577.8$ MPa and the minimum is $E^*_{min} = E^*_{(111)} = 469.0$ MPa.

arbitrarily large positive or negative values of Poisson's ratio could occur along specific directions.

As shown in [65, 12], the extreme values of $\nu^*_{\boldsymbol{n},\mathbf{m}}$ may be searched along the path $ABCA$ on the unit sphere $|\boldsymbol{n}| = 1$, where $A = (1, 0, 0)$, $B = (1/\sqrt{2}, 1/\sqrt{2}, 0)$, $C = (1/\sqrt{3}, 1/\sqrt{3}, 1/\sqrt{3})$ [3]. For each $\boldsymbol{n}$ along this path, the maximum and minimum values are searched with respect to $\boldsymbol{m}$.

Following the analytical formulation developed by Norris [65], we determine the following quantities:

$$\begin{aligned} \nu^* = \nu^*_{(100,-)} &= -0.171\,, \\ \nu^*_{(110,001)} = \frac{2\mu^*\nu^*}{(1+\nu^*)\mu^*_{iso} + (1-\nu^*)\mu^*} &= -0.146\,, \\ \nu^*_{(110,1\bar{1}0)} = \frac{(1+\nu^*)\mu^*_{iso} - (1-\nu^*)\mu^*}{(1+\nu^*)\mu^*_{iso} + (1-\nu^*)\mu^*} &= 2.46 * 10^{-3}\,. \end{aligned} \tag{13}$$

In Fig. 4b, the extreme values of $\nu^*_{\boldsymbol{n},\boldsymbol{m}}$ along the path $ABCA$ are reported, together with ν^*, $\nu^*_{(110,001)}$ and $\nu^*_{(110,1\bar{1}0)}$. As shown in [65], since $\nu^* > -1$ and $\nu^*_{(110,001)} < 0 < \nu^*_{(110,1\bar{1}0)}$, the minimum Poisson's ratio is $\nu^*_{min} = \nu^* = -0.171$. Further, since $-0.5 < \nu^*_{(110,001)} < \nu^*_{(110,1\bar{1}0)}$, the maximum Poisson's ratio is $\nu^*_{max} = \nu^*_{(110,1\bar{1}0)} = 2.46 * 10^{-3}$, which is close to zero. We note two features of the proposed periodic solid: first, the minimum Poisson's ratio ν^* is independent of the transverse direction $\boldsymbol{m}$; second, $\nu^*_{\boldsymbol{n},\boldsymbol{m}} < 0$ almost everywhere, with the exception of a small neighborhood of B and for specific transverse directions $\boldsymbol{m}$.

4 Experimental test

A sample of auxetic porous medium was produced using a 3D printer. The material used for the fabrication of the specimen is PLA (*polylactic acid*), which can be considered isotropic. Standard uniaxial tensile tests with longitudinal and lateral measurements were carried out to determine the Young's modulus and Poisson's ratio of the material, given by $E_m = 3035$ MPa and $\nu_m = 0.35$ respectively. These are the same values used in the calculations of Section 3 for the periodic system and of Section 5 for the finite model.

The specimen is made of $4 \times 4 \times 5$ cells, as shown in Fig. 5a. Therefore, the dimensions of the specimen are 12 cm $\times$ 12 cm $\times$ 15 cm. The same model, illustrated in Fig. 5b, is built and analysed in the finite element software *Comsol Multiphysics*, as described in Section 5.

[3] They correspond to the crystallographic directions (100), (110), (111).

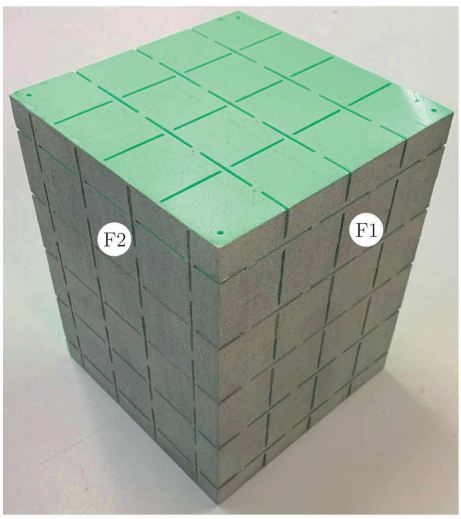

(a)

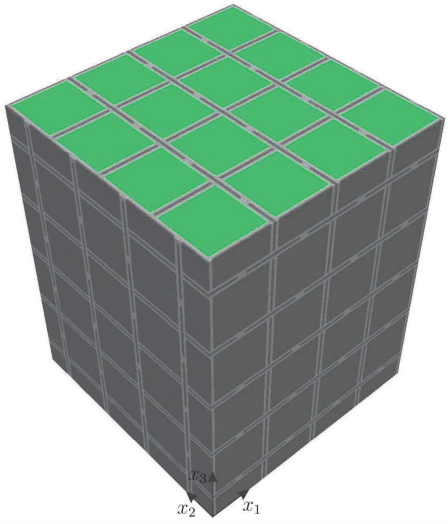

(b)

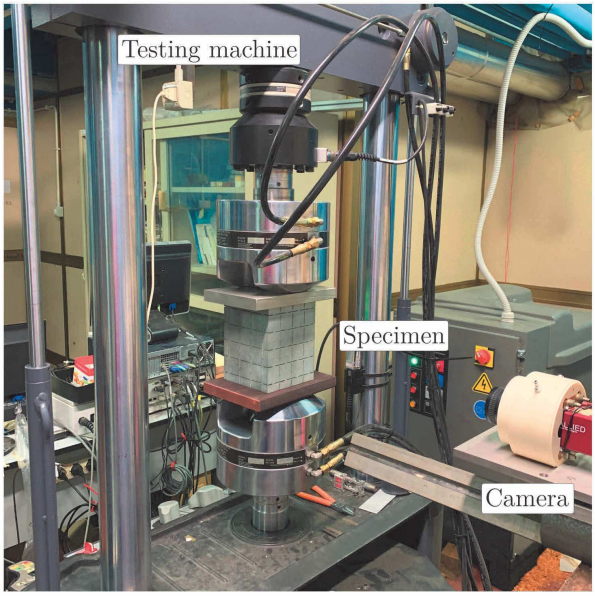

(c)

Figure 5: (a) Specimen manufactured by 3D printing technology using PLA; (b) three-dimensional finite element model developed in *Comsol Multiphysics*; (c) experimental setup, where the sample is subjected to a compressive load and, at each loading step, its surface displacement components are determined by using the DIC (Digital Image Correlation) technique.

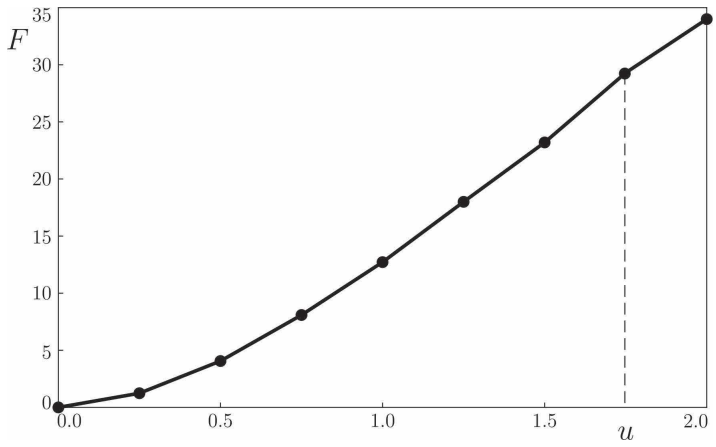

Figure 6: Force-displacement curve for the specimen in Fig. 5a. The compressive force $F = F_3$ is given in kN and the vertical displacement $u = u_3$ in mm. The dashed line indicates the applied displacement corresponding to the DIC colour maps reported in Fig. 7.

4.1 Experimental setup and procedure

The specimen consists of ten 3D printed layers assembled along the x_3-direction. The layers were aligned using cylindrical pins and stuck together with an epoxy glue. Once assembled, the pins were removed and the specimen was painted to realise a speckled surface, as required by DIC (Digital Image Correlation), the experimental technique employed to measure displacements.

The test was performed at the Experimental Mechanics Laboratory of the University of Cagliari using a MTS LandMark 370 universal testing machine. Images were acquired using an AlliedVision F421-B Pike camera (sensor: Kodak IT CCD KAI4021, size 2048 pixel $\times$ 2048 pixel), a Schneider Kreuznach macro camera lens and an isotropic, spot-free professional illuminator. The experimental apparatus adopted to perform the compressive test on the specimen is illustrated in Fig. 5c.

The specimen was loaded under displacement control in the x_3-direction and setting a step increment of 0.25 mm in quasi-static conditions. It was blocked on the upper surface and displaced from below. The load-displacement curve is shown in Fig. 6. It is noted that after an initial nonlinear settling in the displacement range 0.0 mm to 0.75 mm, the specimen displays a linear behavior in the working range.

At each load increment, images of the adjacent frontal and lateral surfaces of the specimen were acquired. The two adjacent faces of the specimen are labeled

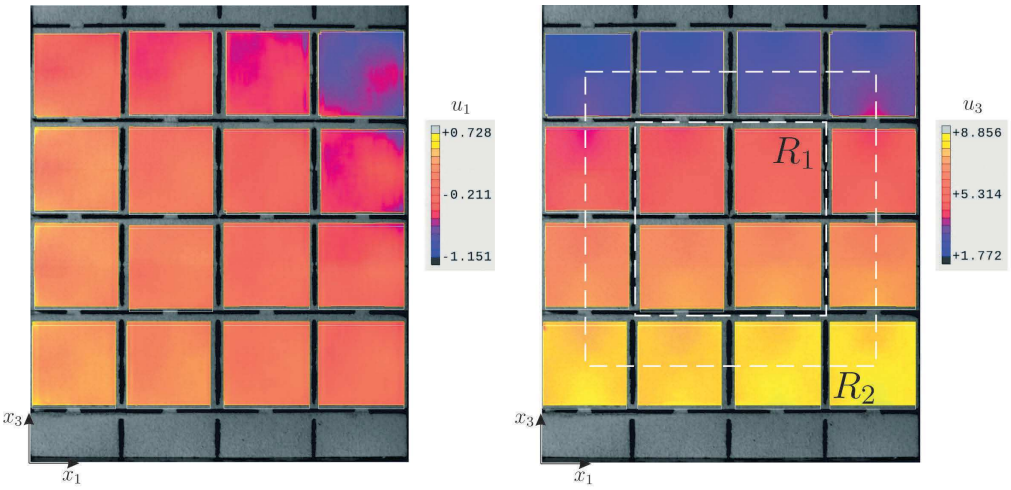

(a) face F1

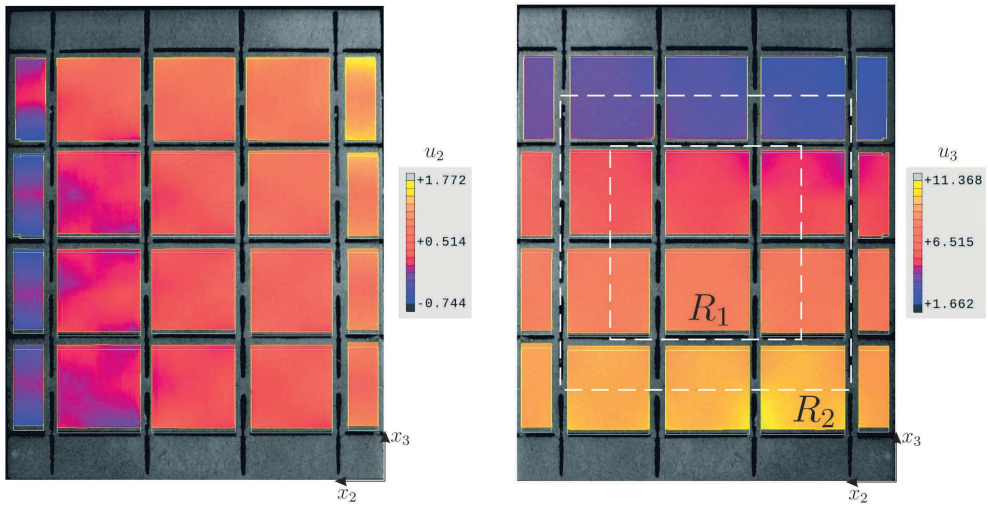

(b) face F2

Figure 7: Colour maps of the displacement components obtained experimentally from DIC: (a) u_1 and u_3 on face F1, parallel to the $x_1 - x_3$ plane; (b) u_2 and u_3 on face F2, parallel to the $x_2 - x_3$ plane. The values are given in pixels on the specimen compressed from below and the results correspond to an applied displacement $u = 1.75$ mm (see Fig. 6). The dashed square regions R_1 and R_2 indicate the 2×2 and 3×3 cell domains, respectively, where the average deformations have been calculated.

as face "F1", parallel to the $x_1 - x_3$ plane, and face "F2", parallel to the $x_2 - x_3$ plane (see Fig. 5a).

An advanced DIC technique [79] has been adopted in order to determine experimentally the displacement components on the faces F1 and F2. Displacements and deformations have been computed using an in-house developed C++ code, described in [6].

The colour maps of the displacement components resulting from the experimental tests at u =1.75 mm are shown in Fig. 7a for face F1 and in Fig. 7b for face F2. From the figures, compression is observed not only in the x_3-direction but also in the x_1- (face F1) and x_2- (face F2) directions, demonstrating the auxeticity of the porous system.

The internal "mechanism" responsible for the negative effective Poisson's ratio is also highlighted in Fig. 8, where the color maps of the rotations are reported. The rotation components $\omega_{31} = (u_{3,1} - u_{1,3})/2$ and $\omega_{23} = (u_{2,3} - u_{3,2})/2$ are shown in Figs. 8a and 8b, respectively, where, in general, $u_{i,j} = \partial u_i / \partial x_j$ $(i, j = 1, 2, 3)$. The contours are obtained from the displacement components evaluated with the DIC analysis. In each square, the compressed specimen undergoes opposite rotations disposed in a checkerboard pattern. Such rotations are kinematically compatible with the flattening of the pores in the proximity of their centres. Note that rotations in Fig. 8 have opposite signs with respect to those in Fig. 1, where a tensile (instead of a compressive) boundary load was applied. In Fig. 1, rotations are kinematically compatible with the bulging of the pores.

4.2 Data analysis

Here, we use the data provided by the DIC technique to statistically evaluate the effective Poisson's ratio of the sample.

The two adjacent faces F1 and F2 of the specimen are examined (see Fig. 5a). For each face we consider the central square region R_1 made of 2×2 cells, indicated with a dashed line in Figure 7. From the DIC data we extrapolate the values of the strain components $\varepsilon_{11} = \varepsilon_{11}(t_i, p_j)$ and $\varepsilon_{22} = \varepsilon_{22}(t_i, p_j)$. The strain components are functions of the loading step t_i $(i = 1, \cdots, N_t$, where $N_t = 8$ is the number of considered loading steps) and of the point p_j $(j = 1, \cdots, N_p$, where N_p is the total number of the observed points belonging to the square region).

We point out that the tested region is taken in the middle part of the specimen to reduce boundary effects. We also note that the first loading steps (u=u_3 in the range 0.0 mm to 0.75 mm) are not considered in the computation of the overall Poisson's coefficient, because the load needs to be large enough to allow for the necessary adjustment of the specimen, as also reported in the discussion of the

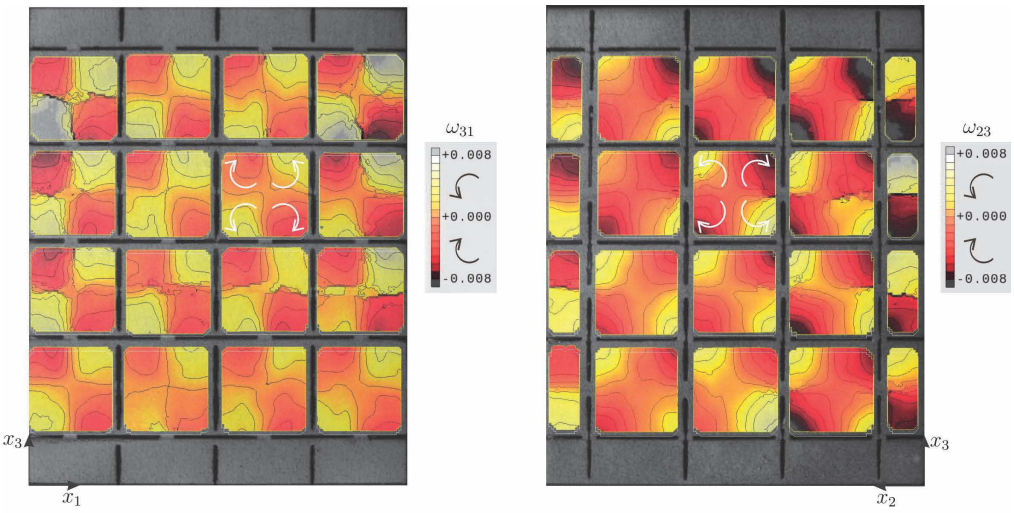

(a) face F1 (b) face F2

Figure 8: Rotations: (a) ω_{31} on face $F1$, (b) ω_{23} on face $F2$. The contour plots are obtained from the DIC displacement measurements. Positive values correspond to anti-clockwise rotations.

force-displacement curve in Fig. 6.

At any loading step t_i $(i = 1, \cdots, N_t)$, the mean of $\nu(t_i, p_j)$ is given by

$$\bar{\nu}(t_i) = -\frac{\bar{\varepsilon}_{11}(t_i)}{\bar{\varepsilon}_{22}(t_i)}\,, \tag{14}$$

where the mean deformations are

$$\bar{\varepsilon}_{11}(t_i) = \sum_{j=1}^{N_p} \eta'_j\, \varepsilon_{11}(t_i, p_j) \quad \text{and} \quad \bar{\varepsilon}_{22}(t_i) = \sum_{j=1}^{N_p} \eta'_j\, \varepsilon_{22}(t_i, p_j)\,, \tag{15}$$

with the weights defined in terms of the cumulative residual as follows

$$\eta'_j = \frac{1/\chi_j^2}{\sum_{i=1}^{N_p} \left(1/\chi_i^2\right)}, \quad (j = 1, \cdots, N_p). \tag{16}$$

The standard error of the mean of $\nu(t_i, p_j)$ is

$$\delta_\nu(t_i) = \frac{\sigma_\nu(t_i)}{\sqrt{N_p}}\,, \tag{17}$$

where

$$\sigma_\nu(t_i) = \sqrt{\mathrm{var}_\nu(t_i)} \tag{18}$$

is the standard deviation of $\nu(t_i, p_j)$ and

$$\begin{aligned} \mathrm{var}_\nu(t_i) =& \mathrm{var}\left(-\frac{\varepsilon_{11}(t_i)}{\varepsilon_{22}(t_i)}\right) \approx \left(-\frac{\bar{\varepsilon}_{11}(t_i)}{\bar{\varepsilon}_{22}(t_i)}\right)^2 \\ & \times \left[\frac{\mathrm{var}(-\varepsilon_{11}(t_i))}{(-\bar{\varepsilon}_{11}(t_i))^2} + \frac{\mathrm{var}(\varepsilon_{22}(t_i))}{(\bar{\varepsilon}_{22}(t_i))^2} - 2\frac{\mathrm{cov}(-\varepsilon_{11}(t_i), \varepsilon_{22}(t_i))}{-\bar{\varepsilon}_{11}(t_i)\bar{\varepsilon}_{22}(t_i)}\right] \end{aligned} \tag{19}$$

is the variance of $\nu(t_i, p_j)$. Hence:

$$\nu(t_i) = \bar{\nu}(t_i) \pm \delta_\nu(t_i)\,. \tag{20}$$

The weighted mean is defined as

$$\bar{\nu} = \frac{\sum_{i=1}^{N_t} w_i\, \bar{\nu}(t_i)}{\sum_{i=1}^{N_t} w_i}\,, \tag{21}$$

where

$$w_i = \frac{1}{\delta_\nu^2(t_i)} \tag{22}$$

is the weight. Applying the formulas of error propagation, we obtain that the error is given by

$$\delta_\nu = \frac{1}{\sqrt{\sum_{i=1}^{N_t} w_i}}\,. \tag{23}$$

Finally, the effective Poisson's ratio of the medium is estimated by the formula:

$$\nu^* = \bar{\nu} \pm \delta_\nu\,. \tag{24}$$

The data corresponding to face F1 and face F2 yield $\nu^* = -0.1268 \pm 0.0024$ and $\nu^* = -0.2000 \pm 0.0018$, respectively. If we consider a region of the specimen made of 3×3 cells (see the domain R_2 in Figure 7), following the same procedure we obtain $\nu^* = -0.1219 \pm 0.0018$ for face F1 and $\nu^* = -0.1807 \pm 0.0016$ for face F2. The average of all the values above is $\nu^* \approx -0.157$.

The experimental data $\nu(t_i)$ at each step on the faces F1 and F2 are reported in Fig. 9, in part (a) and (b) respectively, together with the average values $\nu^* = -0.1268$ and $\nu^* = -0.2000$, indicated with dashed lines. The curves confirm quantitatively the auxeticity of the porous medium.

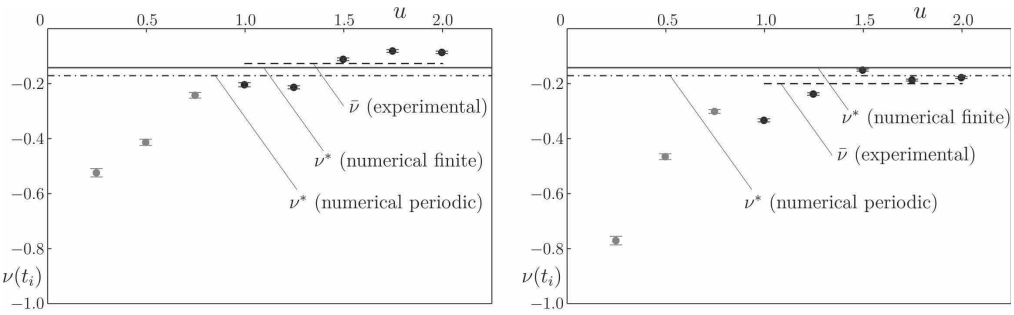

(a) Face F1 (2×2 cells) (b) Face F2 (2×2 cells)

Figure 9: Effective Poisson's ratio $\nu(t_i)$ at each loading step t_i as a function of the applied displacement u (in mm) in the compression test (see Eq. (20)). Values have been computed from DIC data on face (a) F1 and (b) F2. Black dots indicate the data adopted in the computation of the average effective Poisson's ratio ν^*, indicated with a dashed line (see Eq. (24)). Numerical values computed with finite element analyses are also shown: the continuous and dot-dashed lines indicate the results for the finite specimen (Section 5) and for the unit cell in the periodic system (Section 3.1), respectively.

5 Numerical vs experimental model

In this section, we present the results of a finite element model of the specimen and we compare them with the experimental findings reported in Section 4. These numerical simulations embed the effect of the boundary conditions of the finite specimen.

5.1 Numerical simulations for the finite model

The numerical model of the specimen, shown in Fig. 5b, is built in the finite element software *Comsol Multiphysics*. The lower face of the model, parallel to the $x_1 - x_2$ plane, is subjected to a displacement in the x_3-direction equal to $u = u_3 = 1$ mm. In addition, the three components of the displacement on the upper face are prevented. The values of the material and geometrical parameters are identical to those of the real sample, discussed in Section 4. The mesh consists of $7.43 * 10^5$ tetrahedral elements.

A static analysis is performed to determine the components of the stress and strain tensors, evaluated as the average values in the internal $2 \times 2 \times 3$ cells. Eqs. (4) and (5) are used to compute the effective Poisson's ratio and Young's modulus from the average components of the stress and strain tensors; they have been implemented for $i = 1, 2, 3$, leading to the same results up to the third digit,

namely $\nu^* = -0.142$ and $E^* = 652$ MPa, respectively.

The colour maps of the three displacement components are presented in Fig. 10. The effect of the negative Poisson's ratio on the deformation of the structure is very clear: a longitudinal compression of the model in the x_3-direction produces transverse contractions in both the x_1- and x_2-direction. We also stress the good agreement between the experimental and numerical results in Figs. 7 and 10, respectively.

5.2 Summary of numerical and experimental results

The values of the effective Poisson's ratio determined numerically and experimentally are summarised in Table 1. The first column refers to the periodic system examined in Section 3. The second column includes the value of ν^* derived from the finite element analysis of the finite model, discussed in Section 5.1. Finally, the third column presents the effective Poisson's ratio provided by the DIC technique, described in Section 4.

The comparison shows the agreement between the two numerical and the experimental findings. In particular, it is clear that the model presented in this paper is auxetic. Besides, the difference between the periodic and the finite system is an indication of the relative long-range effect of the boundary conditions for this type of microstructured medium. More precisely, the exponentially decaying perturbations induced by the boundary conditions on the fields in the bulk (obtained from the periodic analysis on a unit cell) has a non-negligible effect over more than one unit cell.

Table 1: Effective Poisson's ratio ν^* obtained from the numerical simulations (both for the periodic system and finite model) and from the experimental tests.

	numerical (periodic)	numerical (finite)	experimental
ν^*	-0.171	-0.142	-0.157

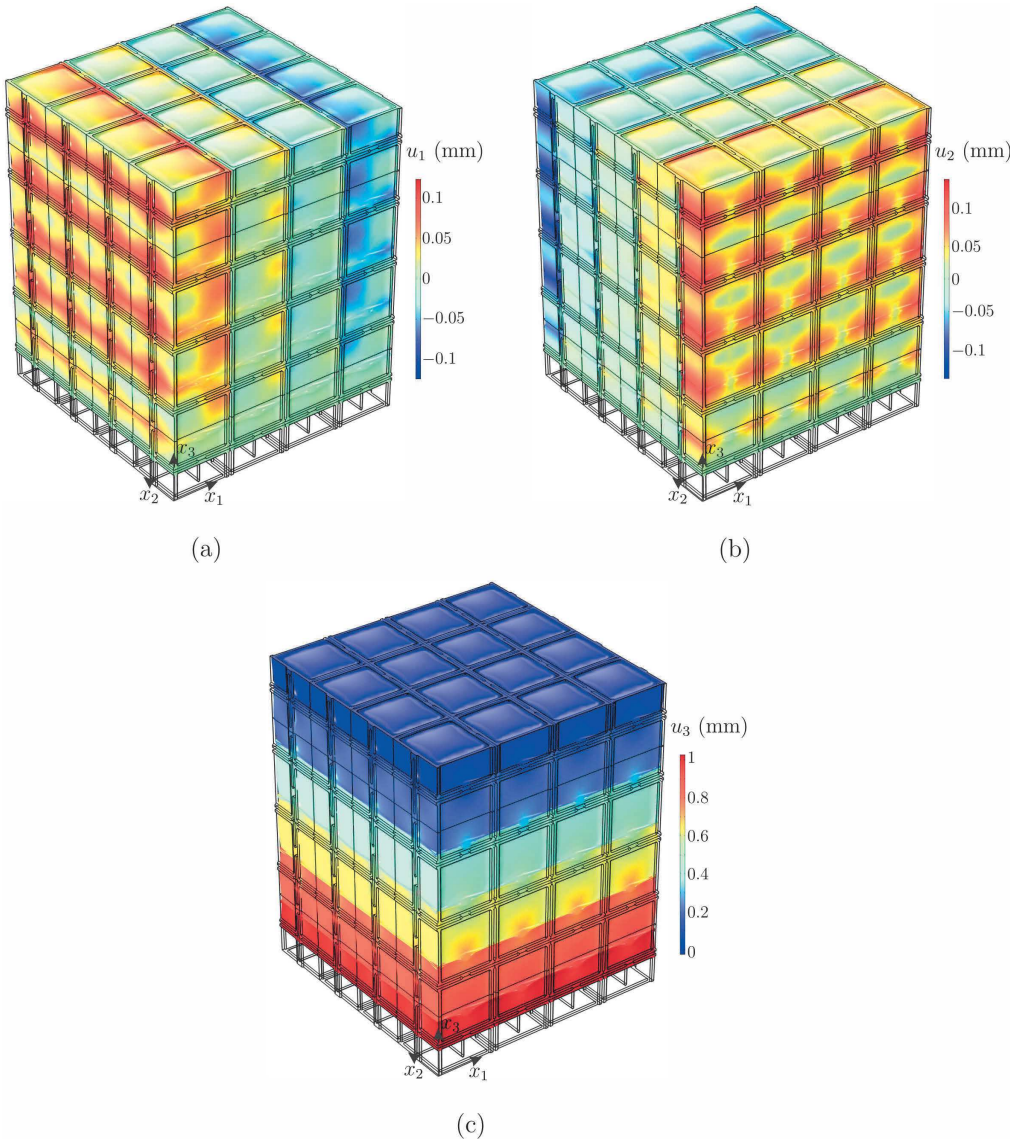

Figure 10: Colour maps of the displacement components obtained from the numerical finite model: (a) displacement u_1 along the x_1-direction; (b) displacement u_2 along the x_2-direction; (c) displacement u_3 along the x_3-direction. Results correspond to an applied displacement $u_3 = 1.00\,\text{mm}$.

6 Voids' dimension versus effective properties

The effective properties of the medium strongly depend on the shape and size of the voids. In this section, we present the results of a parametric study where the relative dimensions of the voids $\tilde{a} = a/(2l)$ and $\tilde{t} = t/(2l)$ (see Fig. 2) are varied and the corresponding effective elastic constants of the medium are determined from (7), (8) and (6). The computations are performed on the unit cell subjected to periodic boundary conditions as in Section 3.

Figures 11a, 11b and 11c show how the effective Poisson's ratio ν^*, the normalised effective Young's modulus E^*/E_m and the normalised effective shear modulus μ^*/μ_m, respectively, vary with the relative size of the voids $\tilde{a}$, for three different values of the relative thickness of the voids $\tilde{t}$, detailed in the diagrams. The stars identify the values of the effective properties corresponding to the particular choice of $\tilde{a}$ and $\tilde{t}$ adopted previously in Sections 3, 4 and 5, namely $\tilde{a} = 0.833$ and $\tilde{t} = 0.042$. The computations are performed for $\tilde{a} < \tilde{a}_{\rm cr}$, where $\tilde{a}_{\rm cr} = 1 - \sqrt{2}\tilde{t}$ denotes the critical value of $\tilde{a}$ at which coalescence of voids is attained.

All the curves in Fig. 11 are monotonically decreasing functions of $\tilde{a}$. Further, from Fig. 11a it is apparent that, for a fixed value of $\tilde{a}$, the effective Poisson's ratio of the medium decreases as the relative thickness $\tilde{t}$ increases. On the contrary, the minimum values of ν^* at coalescence decrease with the decrease of the relative thickness $\tilde{t}$. Concurrently, the effective Young's and shear moduli decrease (see Figs. 11b and 11c).

The dot-dashed lines in Fig. 11b indicate the Hashin-Shtrikmann upper bounds for different thicknesses. The upper bound [40, 41] in terms of the Young's modulus [16] takes the form

$$\frac{E^*_{HS}}{E_m} = \frac{2(1-\phi)(7-5\nu_m)}{2(7-5\nu_m) + (13-2\nu_m-15\nu_m^2)\phi}\,, \tag{25}$$

where the porosity is given by

$$\phi = \tilde{t}(6\tilde{a}^2 + 3\pi\tilde{a}\tilde{t} + \pi\tilde{t}^{\,2})\,. \tag{26}$$

The dashed lines in Fig. 11c represent the normalised effective shear modulus μ^*_{iso}/μ_m of an isotropic medium, where $\mu^*_{iso} = E^*/[2(1+\nu^*)]$. The difference between the solid and dashed curves highlights once more that the porous medium is cubic, but the anisotropy is not "large".

Similar trends can be observed in Figs. 12a, 12b and 12c where ν^*, E^*/E_m and μ^*/μ_m, respectively, are shown as functions of the porosity ϕ. The results

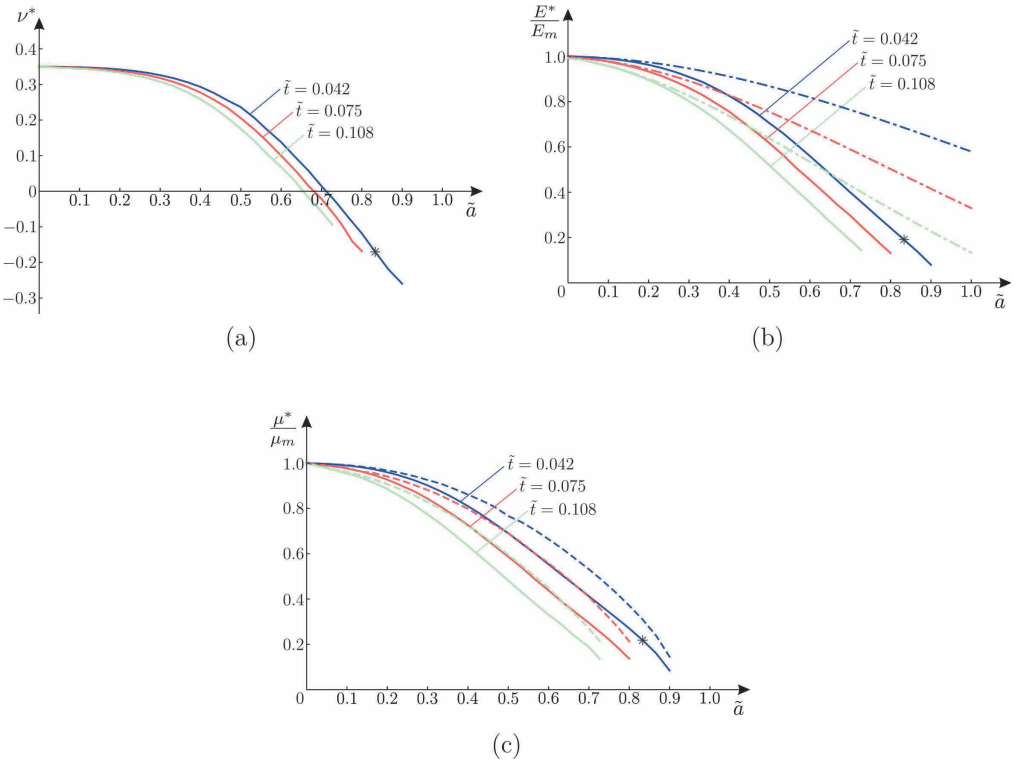

Figure 11: (a) Effective Poisson's ratio, (b) normalised effective Young's modulus and (c) normalised effective shear modulus as functions of $\tilde{a}$. The curves correspond to three values of $\tilde{t}$, specified in the figures. The stars indicate the values of the effective elastic constants obtained for the particular case considered in Section 3. In (b), the dot-dashed lines indicate the Hashin-Shtrikman upper bounds for different thicknesses. In (c), the dashed lines represent the values of the normalised shear modulus μ^*_{iso}/μ_m of the corresponding isotropic medium (see Eq. (9)).

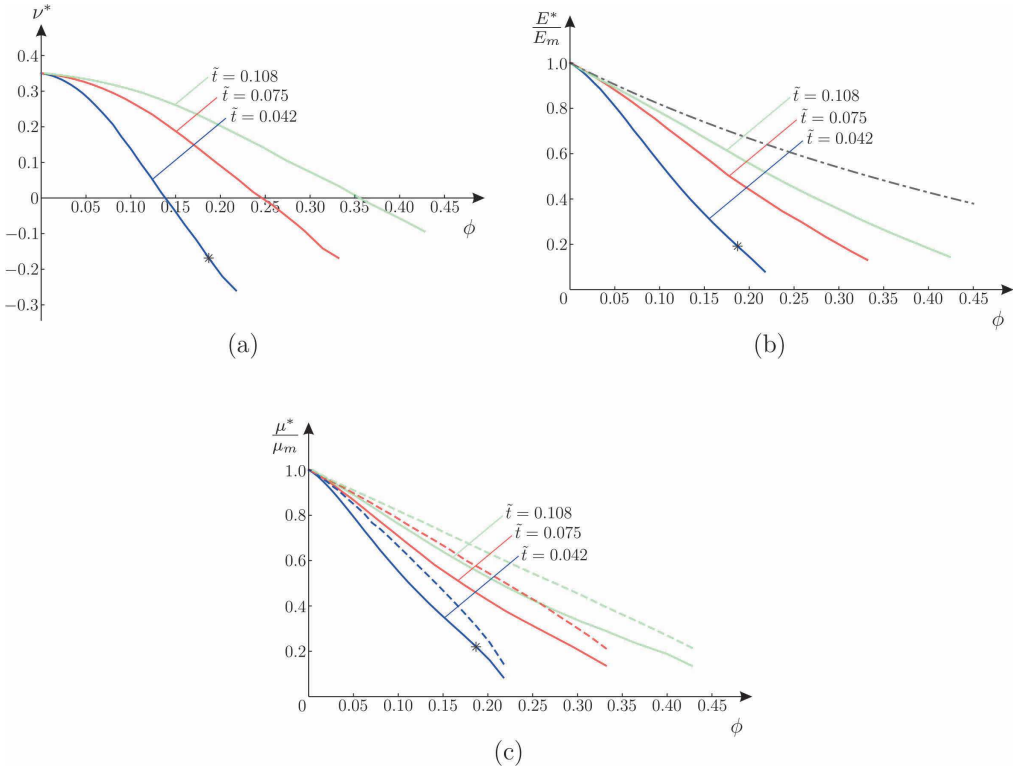

Figure 12: (a) Effective Poisson's ratio, (b) normalised effective Young's modulus and (c) normalised effective shear modulus as functions of the porosity ϕ, defined in (26), for three values of the relative thickness $\tilde{t}$. The stars indicate the values of the effective elastic constants obtained for the choice of parameters considered in Section 3, for which $\phi = 0.187$. In (b) the dot-dashed line indicates the Hashin-Shtrikman upper bound. In (c), the dashed lines represent the values of the normalised shear modulus μ^*_{iso}/μ_m of the corresponding isotropic medium.

in Figures 12 reveal that the effective elastic constants depend not only on the porosity, but also on the shape of the voids, that can be linked to the relative thickness $\tilde{t}$.

7 Conclusions

The periodic medium presented in this work is a porous continuous system with a fully 3D distribution of void inclusions. The macroscopic negative Poisson's ratio derives from the design of the microstructure, which has cubic symmetry and moderate degree of anisotropy. The numerical and experimental results are in good agreement and demonstrate the *auxeticity* of the medium.

The negative Poisson's ratio is comparable to that of the three-dimensional woven fabric in [44]. Simultaneously, the medium is characterised by low porosity and large relative Young's modulus; hence, it is suitable for technological applications where the structural performance in terms of rigidity is desirable.

The relative Young's modulus E^*/E_m is about 16%, one order of magnitude larger than the relative Young's modulus of the lattice model in [58] (where $E^*/E_m < 1,6\%$) and more than two orders of magnitude larger than that of the design in [86] ($E^*/E_m \simeq 0.2\%$ in the highest case). Concerning foams, Gibson and Ashby showed that the relative Young's modulus scales as $(A/L^2)^2$ (see [57]), where A is the cross-sectional area and L is the length of the internal ribs, leading to values of the relative Young's modulus that are several orders of magnitude smaller than the Young's modulus of the proposed porous system.

The model presented in this paper represents a new class of three-dimensional porous composite materials beyond lattice, cellular, chiral and origami auxetic media, that can be useful in novel technological applications for large-scale production.

In a future work, we aim to carry out a thorough optimisation of the geometrical parameters of the system, in order to minimise the Poisson's coefficient controlling the corresponding reduction of the effective stiffness of the microstructured material. In addition, we plan to analyse the effects of constitutive and geometrical nonlinearities both in traction and compression, where the second loading condition is expected to cause partial closure of internal voids over a certain threshold.

Acknowledgements The financial support of Regione Autonoma della Sardegna, project ADVANCING, CUP F74I19001030007 is gratefully acknowledged (M.B.).

References

[1] Albag OE (2021). Auxetic Materials. In: Paoletti I., Nastri M. (eds) Material Balance. *Springer Briefs Appl. Sci. Tech.*, 65–74.

[2] Alderson A, Rasburn J and Evans KE (2007). Mass transport properties of auxetic (negative Poisson's ratio) foams. *Phys. Status Solidi B*, **244**(3), 817–827. doi: 10.1002/pssb.200572701

[3] Andreassen E, Lazarov BS and Sigmund O (2014). Design of manufacturable 3d extremal elastic microstructure. *Mech. Mat.*, **69**(1), 1–10. doi: 10.1016/j.mechmat.2013.09.018

[4] Babaee S, Shim J, Weaver JC, Chen ER, Patel N and Bertoldi K (2013). 3D Soft Metamaterials with Negative Poisson's Ratio. *Adv. Mater.*, **25**(36), 5044–5049. doi: 10.1002/adma.201301986

[5] Bacigalupo A and Gambarotta L (2020). Chiral two-dimensional periodic blocky materials with elastic interfaces: Auxetic and acoustic properties. *Extreme Mech. Lett.*, **39**, 100769. doi: 10.1016/j.eml.2020.100769

[6] Baldi A and Bertolino F (2016). Assessment of h-refinement procedure for global digital image correlation. *Meccanica*, **51**(4), 979-991. doi: 10.1007/s11012-015-0253-6

[7] Baughman RH, Shacklette JM, Zakhidov AA and Stafström S (1998). Negative Poisson's ratio as a common feature of cubic metals. *Nature*, **392**, 362–365. doi: 10.1038/32842

[8] Bertoldi K, Reis PM, Willshaw S and Mullin T (2010). Negative Poisson's ratio behavior induced by an elastic instability. *Adv. Mater.*, **22**(3), 361–366. doi: 10.1002/adma.200901956

[9] Bianchi M, Scarpa F and Smith C (2008). Stiffness and energy dissipation in polyurethane auxetic foams. *J. Mater. Sci.*, **43**(17), 5851–5860. doi: 10.1007/s10853-008-2841-5

[10] Bonfanti A, Syngellakis S and Bhaskar A (2020). Structural analysis of cyclically periodic rings and its application to the mechanics of balloon expandable stents. *Int. J. Solids Struct.*, **185–186**, 45–56. doi: 10.1016/j.ijsolstr.2019.04.005

[11] Cabras L and Brun M (2014). Auxetic two-dimensional lattices with Poisson's ratio arbitrarily close to -1. *Proc. R. Soc. London A*, **470**(2172), 20140538. doi: 10.1098/rspa.2014.0538

[12] Cabras L and Brun M (2016). A class of auxetic three-dimensional lattices. *J. Mech. Phys. Solids*, **91**, 56–72. doi: 10.1016/j.jmps.2016.02.010

[13] Cabras L, Brun M and Misseroni D (2019). Micro-structured medium with large isotropic negative thermal expansion. *Proc. R. Soc. London A*, **475**(2232), 20190468. doi: 10.1098/rspa.2019.0468

[14] Carta G, Brun M and Baldi A (2016). Design of a porous material with isotropic negative Poisson's ratio. *Mech. Mat.*, **97**, 67–75. doi: 10.1016/j.mechmat.2016.02.012

[15] Carta G, Cabras L and Brun M (2016). Continuous and discrete microstructured materials with null Poisson's ratio. *J. Eur. Ceram. Soc.*, **63**(9), 2183–2192. doi: 10.1016/j.jeurceramsoc.2016.01.003

[16] Casnedi L, Licheri R, Brun M and Pia G (2020). From nature geometry to material design: Advanced fractal nature analysis for predicting experimental elastic properties. *Ceram. Int.*, **46**(15), 23947–23955. doi: 10.1016/j.ceramint.2020.06.171

[17] Chen X, Moughames J, Li Q, Martínez JAI, Tan H, Adrar S, Laforge N, Cote JM, Euphrasie S, Ulliac G, Kadic M and Laude V (2020). Optimal isotropic, reusable truss lattice material with near-zero Poisson's ratio. *Extreme Mech. Lett.*, **41**, 101048. doi: 10.1016/j.eml.2020.101048

[18] COMSOL Multiphysics®v. 5.3. www.comsol.com. COMSOL AB, Stockholm, Sweden.

[19] Davini C, Favata A, Micheletti A and Paroni R (2017). A 2D microstructure with auxetic out-of-plane behavior and non-auxetic in plane behavior. *Smart Mater. Struct.*, **26**(12), 125007. doi: 10.1088/1361-665X/aa9091

[20] De Bellis ML and Bacigalupo A (2017). Auxetic behavior and acoustic properties of microstructured piezoelectric strain sensors. *Smart Mater. Struct.*, **26**(8), 085037. doi: 10.1088/1361-665X/aa7772

[21] Derrouiche A, Zaïri F and Zaïri F (2019). A chemo-mechanical model for osmo-inelastic effects in the annulus fibrosus. *Biomech. Model. Mechanobiol.*, **18**, 1773–1790. doi: s10237-019-01176-8

[22] Donoghue J, Alderson K and Evans K (2009). The fracture toughness of composite laminates with a negative Poisson's ratio. *Phys. Status Solidi B*, **246**(9), 2011–2017. doi: 10.1002/pssb.200982031

[23] Doyoyo M and Hu JW (2006). Plastic failure analysis of an auxetic foam or inverted strut lattice under longitudinal and shear loads. *J. Mech. Phys. Solids*, **54**(7), 1479–1492. doi: 10.1016/j.jmps.2005.12.007

[24] Duncan O, Foster L, Senior T, Alderson A and Allen T (2016). Quasi-static characterisation and impact testing of auxetic foam for sports safety applications. *Smart Mater. Struct.*, **25**(5), 054014. doi: 10.1088/0964-1726/25/5/054014

[25] Evans KE (1991). Auxetic polymers: a new range of materials. *Endeavour*, **15**, 170–174. doi: 10.1016/0160-9327(91)90123-S

[26] Evans KE and Alderson A (2000). Auxetic materials: functional materials and structures from lateral thinking! *Adv. Mater.*, **12**, 617–28. doi: 10.1002/(SICI)1521-4095(200005)12:9<617::AID-ADMA617>3.0.CO;2-3

[27] Evans KE, Nkansah MA, Hutchinson IJ and Rogers SC (1991). Molecular network design. *Nature*, **353**, 124. doi: 10.1038/353124a0

[28] Francesconi L, Baldi A, Liang X, Aymerich F and Taylor M (2019). Variable Poisson's ratio materials for globally stable static and dynamic compression resistance. *Exp. Mech.*, **26**, 1–7. doi: 10.1016/j.eml.2018.11.001

[29] Francesconi L, Baldi A, Dominguez G and Taylor M (2020). An Investigation of the Enhanced Fatigue Performance of Low-porosity Auxetic Metamaterials. *Exp. Mech.*, **60**(1), 93–107. doi: 10.1007/s11340-019-00539-7

[30] Gao Y, Zhou Z, Hu H and Xiong J (2021). New concept of carbon fiber reinforced composite 3D auxetic lattice structures based on stretching-dominated cells. *Mech. Mat.*, **152**, 103661. doi: 10.1016/j.mechmat.2020.103661

[31] Gatt R, Vella Wood M, Gatt A, Zarb F, Formosa C, Azzopardi KM, Casha A, Agius TP, Schembri-Wismayer P, Attard L, Chockalingam N and Grima JN (2015). Negative Poisson's ratios in tendons: An unexpected mechanical response. *Acta Biomater.*, **24**, 201–208. doi: 10.1016/j.actbio.2015.06.018

[32] Gibson LJ and Ashby MF (1997). *Cellular Solids*. Cambridge University Press, London, UK.

[33] Greaves G, Greer A, Lakes R and Rouxel T (2011). Poisson's ratio and modern materials. *Nat. Mater.*, **10**(11), 823–837. doi: 10.1038/nmat3134

[34] Grima JN, Alderson A and Evans KE (2005). Auxetic behaviour from rotating rigid units. *Phys. Status Solidi B*, **242**(3), 561–575. doi: 10.1002/pssb.200460376

[35] Grima JN, Gatt R and Farrugia PS (2008). On the properties of auxetic meta-tetrachiral structures. *Phys. Status Solidi B*, **245**(3), 511–520. doi: 10.1002/pssb.200777704

[36] Grima JN and Gatt R (2010). Perforated sheets exhibiting negative Poisson's ratios. *Adv. Eng. Mater.*, **12**(6), 460–464. doi: 10.1002/adem.201000005

[37] Gunton DD and Saunders GA (1972). The Young's modulus and Poisson's ratio of arsenic, antimony and bismuth. *J. Mater. Sci.*, **7**, 1061–1068. doi: 10.1007/BF00550070

[38] Ha CS, Hestekin E, Li J, Plesha ME and Lakes RS (2015). Controllable thermal expansion of large magnitude in chiral negative Poisson's ratio lattices. *Phys. Status Solidi B*, **252**(7), 1431–1434. doi: 10.1002/pssb.201552158

[39] Harris JA and McShane GJ (2021). Impact response of metallic stacked origami cellular materials. *Int. J. Impact Eng.*, **147**, 103730. doi: 10.1016/j.ijimpeng.2020.103730

[40] Hashin Z and Shtrikman S (1962). On some variational principles in anisotropic and non-homogeneous elasticity. *J. Mech. Phys. Solids*, **10**, 335–342. doi: 10.1016/0022-5096(62)90004-2

[41] Hashin Z and Shtrikman S (1963). A variational approach to the theory of the elastic behaviour of multiphase materials. *J. Mech. Phys. Solids*, **11**, 127–140. doi: 10.1016/0022-5096(63)90060-7

[42] Howell B, Prendergast P and Hansen L (1994). Examination of acoustic behavior of negative Poisson's ratio materials. *Appl. Acoust.*, **43**(2), 141–148. doi: 10.1016/0003-682X(94)90057-4

[43] Industry Growth Inside. https://industrygrowthinsights.com/report/particulate-reinforced-composites-market/ (accessed 15 September 2021).

[44] Iftekhar H, Ullah Khan RMW, Nawab Y, Hamdani STA and Panchal S (2020). Numerical Analysis of Binding Yarn Float Length for 3D Auxetic Structures. *Phys. Status Solidi B*, **257**(10), 2000440. doi: 10.1002/pssb.202000440

[45] Kursumovic A, Defay E, Lee OJ, Tsai CF, Bi Z, Wang H and MacManus-Driscoll JL (2013). A New Material for High-Temperature Lead-Free Actuators. *Adv. Funct. Mater.*, **23**(47), 5881–5886. doi: 10.1002/adfm.201300899

[46] Lakes RS (1987). Foam structures with a negative Poisson's ratio. *Science*, **253**(4792), 1038–1040. doi: 10.1126/science.235.4792.1038

[47] Lakes RS and Elms K (1993). Indentability of conventional and negative Poisson's ratio foams. *J. Compos. Mater.*, **27**(12), 1193–1202. doi: 10.1177/002199839302701203

[48] Lakes RS (2017). Negative-Poisson's-Ratio Materials: Auxetic Solids. *Ann. Rev. Mater. Res.*, **47**, 63–81. doi: 10.1146/annurev-matsci-070616-124118

[49] Larsen UD, Sigmund O and Bouwsta S (1997). Design and fabrication of compliant micromechanisms and structures with negative Poisson's ratio. *J. Microelectromech. Syst.*, **6**(2), 99–106. doi: 10.1109/84.585787

[50] Lazarus A and Reis PM (2015). Soft actuation of structured cylinders through auxetic behavior. *Adv. Rev. Mater.*, **17**(6), 815–820. doi: 10.1002/adem.201400433

[51] Lee Y, Kim J, Jang B, Kim S, Sharma BK, Kim JH and Ahn JH (2019). Graphene-based stretchable/wearable self-powered touch sensor. *Nano Energy*, **62**, 197–204. doi: 10.1016/j.nanoen.2019.05.04

[52] Lees C, Vincent JF and Hillerton JE (1991). Poisson's ratio in skin. *Biomed. Mater. Eng.*, **1**(1), 19–23. doi: 10.3233/BME-1991-1104

[53] Li Y (1976). The anisotropic behavior of Poisson's ratio, Young's modulus, and shear modulus in hexagonal materials. *Phys. Status Solidi A*, **38**, 171–175. doi: 10.1002/pssa.2210380119

[54] Li X, Wang Q, Yang Z and Lu Z (2019). Novel auxetic structures with enhanced mechanical properties. *Extreme Mech. Lett.*, **27**, 59–65. doi: 10.1016/j.eml.2019.01.002

[55] Liu J, Yao X, Wang Z, Yec J, Luan C, He Y, Lin H and Fu J (2021). A flexible porous chiral auxetic tracheal stent with ciliated epithelium. *Acta Biomater.*, **124**, 153–165. doi: 10.1016/j.actbio.2021.01.044

[56] Love AEH (1944). *A treatise on the mathematical theory of elasticity*, 4th edn. Dover Publications, New York, USA.

[57] Lu ZX, Liu Q, and Yang ZY (2011). Predictions of Young's modulus and negative Poisson's ratio of auxetic foams. *Phys. Status Solidi B*, **248**(1), 167–174. doi: 10.1002/pssb.201046120

[58] Lu Z, Wang Q, Li X and Yang Z (2017). Elastic properties of two novel auxetic 3D cellular structures. *Int. J. Solids Struct.*, **124**, 46–56. doi: 10.1016/j.ijsolstr.2017.05.031

[59] Mardling P, Alderson A, Jordan-Mahy N and Le Maitre CL (2020). The use of auxetic materials in tissue engineering. *Biomater. Sci.*, **8**, 2074–2083. doi: 10.1039/c9bm01928f

[60] Milton GW (2013). Complete characterization of the macroscopic deformations of periodic unimode metamaterials of rigid bars and pivots. *J. Mech. Phys. Solids*, **61**, 1543–1560. doi: 10.1016/j.jmps.2012.08.011

[61] Milton GW (2013). Adaptable nonlinear bimode metamaterials using rigid bars, pivots, and actuators. *J. Mech. Phys. Solids*, **61**, 1561–1568. doi: 10.1016/j.jmps.2012.08.012

[62] Mizzi L, Attard D, Casha A, Grima JN and Gatt R (2014). On the suitability of hexagonal honeycombs as stent geometries. *Phys. Statu Solidi B*, **251**(2), 328–337. doi: 10.1002/pssb.201384255

[63] Mizzi L, Mahdi EM, Titov K, Gatt R, Attard D, Evans KE, Grima JN and Tan J-C (2018). Mechanical metamaterials with star-shaped pores exhibiting negative and zero Poisson's ratio. *Mater. Des.*, **146**, 28–37. doi: 10.1016/j.matdes.2018.02.051

[64] Morvaridi M, Carta G, Bosia F, Gliozzi AS, Pugno N, Misseroni D and Brun M (2021). Hierarchical auxetic and isotropic porous medium with extremely negative Poisson's ratio. *Extreme Mech. Lett.*, **48**, 101405. doi: 10.1016/j.eml.2021.101405

[65] Norris AN (2006). Poisson's ratio in cubic materials. *Proc. R. Soc. A*, **462**(275), 3385–3405. doi: 10.1098/rspa.2006.1726

[66] Oh J, Kim J, Nguyen V and Oh I (2020). Auxetic graphene oxide-porous foam for acoustic wave and shock energy dissipation. *Compos. B Eng.*, **186**, 107817. doi: 10.1016/j.compositesb.2020.107817

[67] Peng XL, Soyarslan C and Bargmann S (2020). Phase contrast mediated switch of auxetic mechanism in composites of infilled re-entrant honeycomb microstructures. *Extreme Mech. Lett.*, **35**, 100641. doi: 10.1016/j.eml.2020.100641

[68] Poisson SD (1829). Mémoire sur l'équilibre et le mouvement des corps élastiques. *Paris., Mém. de l'Acad.*, 8.

[69] Prall D and Lakes RS (1997). Properties of a chiral honeycomb with a Poisson's ratio of -1. *Int. J. Mech. Sci.*, **39**, 305–307, 309–314. doi: 10.1016/S0020-7403(96)00025-2

[70] Qi D, Lu Q, Wang C, He CW, Li Y, Wu W and Xiao D (2019). Impact energy absorption of functionally graded chiral honeycomb structures. *Extreme Mech. Lett.*, **32**, 100568. doi: 10.1016/j.eml.2019.100568

[71] Raminhos JS, Borges JP and Velhinho A (2019). Development of polymeric anepectic meshes: auxetic metamaterials with negative thermal expansion. *Smart Mater. Struct.*, **28**, 045010. doi: 10.1088/1361-665X/ab034b

[72] Saxena KK, Das R and Calius EP (2016). Three decades of auxetics research - Materials with negative Poisson's ratio: A Review. *Adv. Eng. Mater.*, **18**(11), 1847–1870. doi: 10.1002/adem.201600053

[73] Shan S, Kang SH, Zhao Z, Fang L and Bertoldi K (2015). Design of planar isotropic negative Poisson's ratio structures. *Extreme Mech. Lett.*, **4**, 96–102. doi: 10.1016/j.eml.2015.05.002

[74] Shen J, Zhou S, Huang X and Xie YM (2014). Simple cubic three-dimensional auxetic metamaterials. *Phys. Status Solidi B*, **251**(8), 1515–1522. doi: 10.1002/pssb.201451304

[75] Sigmund O (1995). Tailoring materials with prescribed elastic properties. *Mech. Mat.*, **20**(4), 361–368. doi: 10.1016/0167-6636(94)00069-7

[76] Sigmund O and Torquato S (1997). Design of materials with extreme thermal expansion using a three-phase topology optimization method. *J. Mech. Phys. Solids*, **45**(6), 1037–1067. doi: 10.1016/S0022-5096(96)00114-7

[77] Song L, Ahmed MF, Li Y, Zeng C and Li Y (2018). Vascular differentiation from pluripotent stem cells in 3-D auxetic scaffolds. *J. Tissue Eng. Regener. Med.*, **12**, 1679–1689. doi: 10.1002/term.2695

[78] Spadoni A and Ruzzene M (2012). Elasto-static micropolar behavior of a chiral auxetic lattice. *J. Mech. Phys. Solids*, **60**(1), 156–171. doi: 10.1016/j.jmps.2011.09.012

[79] Sutton MA, Orteu JJ and Schreier H (2009). *Image Correlation for Shape, Motion and Deformation Measurements: Basic Concepts,Theory and Applications*. Springer, New York, USA.

[80] Taylor M, Francesconi L, Gerends M, Shanian A, Carson C and Bertoldi K (2014). Low porosity metallic periodic structures with negative Poisson's ratio. *Adv. Mater.*, **26**(15), 2365–2370. doi: 10.1002/adma.201304464

[81] Theocaris P, Stavroulakis G and Panagiotopoulos P (1997). Negative Poisson's ratios in composites with star-shaped inclusions: a numerical homogenization approach. *Arch. Appl. Mech.*, **67**, 274–286. doi: 10.1007/s004190050117

[82] Timmins LH, Wu Q, Yeh AT, Moore JE and Greenwald SE (2010). Structural inhomogeneity and fiber orientation in the inner arterial media. *Am. J. Physiol. Heart Circ. Physiol.*, **298**(5), 1537–1545. doi: 10.1093/qjmamj/hbh021

[83] Ting TCT and Chen T (2005). Poisson's ratio for anisotropic elastic materials can have no bounds. *Quart. J. Mech. Appl. Math.*, **58**(1), 73–82. doi: 10.1093/qjmamj/hbh021

[84] Veronda DR and Westmann RA (1970). Mechanical characterization of skin-finite deformations. *J. Biomech.*, **3**(1), 111–122. doi: 10.1016/0021-9290(70)90055-2

[85] Wang L, Tan X, Zhu S, Wang B, Li S, Zou Y and Chen S (2021). Directional instability-driven strain-dependent 3D auxetic metamaterials. *Int. J. Mech. Sci.*, **199**, 106408. doi: 10.1016/j.ijmecsci.2021.10640

[86] Wang XT, Wang B, Wen ZH and Ma L (2018). Fabrication and mechanical properties of CFRP composite three-dimensional double-arrowhead auxetic structures. *Compos. Sci. Technol.*, **164**, 92-102. doi: 10.1016/j.compscitech.2018.05.014

[87] Warner JJ, Gillies AR, Hwang HH, Zhang H, Lieber RL and Chen S (2017). 3D-printed biomaterials with regional auxetic properties. *J. Mech. Behav. Biomed. Mater.*, **76**, 145–152. doi: 10.1016/j.jmbbm.2017.05.016

[88] Wiebe C and Brodland GW (2005). Tensile properties of embryonic epithelia measured using a novel instrument. *J. Biomech.*, **38**, 2087–2094. doi: 10.1016/j.jbiomech.2004.09.005

[89] Williams JL and Lewis JL (1982). Properties and an anisotropic model of cancellous bone from the proximal tibial epiphysis. *J. Biomech. Eng.*, **104**(1), 50–56. doi: 10.3390/ma14040993

[90] Zener C (1948). *Elasticity and Anelasticity of Metals*. University of Chicago Press, Chicago, USA.

[91] Zhang J, Jiang D, Scarpa F and Peng H (2013). Enhancement of pull-out energy in a single-walled carbon nanotube-polyethylene composite system via auxetic effect. *Compos. Appl. Sci. Manuf.*, **55**, 188–194. doi: 10.1016/j.compositesa.2013.09.006

[92] Zhang J, Lu G, and You Z (2020). Large deformation and energy absorption of additively manufactured auxetic materials and structures: A review. *Compos. B. Eng.*, **201**, 108340. doi: 10.1016/j.compositesb.2020.108340